JOURNAL OF PROPULSION AND POWER
Vol. 25, No. 5, September–October 2009

Operation of an Annular Helicon Plasma Source

Douglas D. Palmer* and Mitchell L. R. Walker†
Georgia Institute of Technology, Atlanta, Georgia 30332

DOI: 10.2514/1.41403

The plasma parameters of a nominally 1.5 kW annular helicon plasma source are measured and its feasibility as an ionization stage of a two-stage Hall thruster is investigated. All experiments are performed in a 4 by 7 m stainless steel vacuum chamber at pressures below 3.1×10^{-5} torr for argon and 5.6×10^{-5} torr for xenon. Ion number density, electron temperature, and electron energy distribution function measurements are taken at several axial and radial locations inside the device at each operating condition with a ratio-frequency-compensated Langmuir probe. The annular helicon plasma source is characterized over a range of applied radio frequencies (2–14 MHz), magnetic field strengths (0–400 G), and radio frequency forward-power settings (100–1400 W) for both argon and xenon propellants. The peak ion number density measured in the annular helicon is 2.6×10^{17} m^{-3} for argon and 2.4×10^{17} m^{-3} for xenon at 1000 W of radio frequency power. The annular helicon electron energy distribution function peak and shape vary with the radio frequency, from a minimum of 3.7 eV at 13 MHz to a maximum of 15.0 eV at 11 MHz for argon propellant over the preceding operating conditions.

Nomenclature

P_{input}	=	input power
P_{jet}	=	jet power
V_D	=	discharge voltage
V_{nc}	=	neutralizer coupling voltage
γ	=	plume divergence coefficient
ε	=	ionization cost
η	=	efficiency
η_u	=	propellant utilization efficiency

I. Introduction

TWO-STAGE Hall-effect thrusters (HETs), which decouple the ionization stage from the acceleration stage, could achieve a higher efficiency in high-thrust, low-specific-impulse operation than single-stage HETs. The efficiency of an electrostatic acceleration device, which is defined as a ratio of the jet power to input power, is expressed as [1]

$$\eta = \frac{P_{\text{thrust}}}{P_{\text{input}}} = \frac{\eta_u \gamma}{1 + [(\varepsilon + V_{\text{nc}})/V_D]} \tag{1}$$

where η_u is the propellant utilization efficiency,γ is the plume divergence coefficient, ε is the ionization cost, V_{nc} is the neutralizer coupling voltage, and V_D is the discharge voltage. High-thrust-to-power operation requires a high propellant mass flow at a low discharge voltage (100–150 V) [2]. However, Eq. (1) shows that the efficiency of HET decreases as the discharge voltage decreases, because a large fraction of the input power is spent on ionization. Therefore, a method to improve the efficiency of the HET in a high-thrust-to-power operating condition is to replace the dc electron bombardment ionization stage with a more efficient helicon ionization source [3]. Two-stage HETs, which have separate ionization and acceleration stages, have been investigated in the past, but a helicon source has never been used as the ionization stage [1,4–15]. For a helicon source to serve as the ionization stage of a two-stage HET, it must produce steady-state plasma with an ion number density and electron temperature appropriate for the acceleration stage. Past investigations show that the xenon HET acceleration stage requires an inlet ion number density in the range of 1.2×10^{17} to 1.6×10^{18} m^{-3} [16–18].

A helicon plasma source is a high-density, high-efficiency plasma source that sustains steady plasma production through absorption and propagation of helicon waves [19]. The wave is launched by sending RF waves along an applied axial magnetic field [20–23]. A cylindrical helicon source is not readily incorporated into the annular discharge chamber of a HET. However, if a helicon plasma can be excited in a coaxial configuration, the source can feed a high-density plasma into the acceleration stage of a HET and other coaxial accelerators [24]. The theoretical existence of annularly bounded helicon waves is discussed by Yano and Walker [25].

The annular helicon (AH) theoretical model and trade studies indicate that the plasma number densities required by a two-stage HET are attainable in this configuration [23]. Recent works show that the AH reliably produces plasma throughout the regime of interest with RF power in the 7–14 MHz RF range at magnetic field strengths of 0–400 G [21,23]. This research effort characterizes the plasma source as a function of axial and radial locations, RF forward power, magnetic field, mass flow rate, and RF.

II. Experimental Apparatus

A. Facility

All experiments are performed in the vacuum test facility (VTF), a stainless steel vacuum chamber with a diameter of 4 m and a length of 7 m. Two 3800 ft^3/min blowers and two 495 ft^3/min rotary-vane pumps evacuate the facility to moderate vacuum (30 mtorr). To reach high vacuum (10^{-7} torr), the VTF employs six 48 in. diffusion pumps. The VTF pumping speed is varied by changing the number of diffusion pumps in operation. The combined pumping speed of the facility is 600,000 liter/s on air and 155,000 liter/s on xenon, with a base pressure of 1.2×10^{-4} Pa (9.5×10^{-7} torr).

A Varian model UHV-24 ionization gauge with a Varian senTorr vacuum gauge controller monitors the chamber pressure. The UHV-24 ionization gauge is calibrated for air by the manufacturer. The ionization gauge measures pressure over the range of 10^{-2} Pa (10^{-4} torr) to 10^{-10} Pa (10^{-12} torr) with an accuracy of $\pm 20\%$.‡ The VTF also uses a tubulated Kurt J. Lesker Company (KJLC) model

Presented as Paper 4926 at the 44th AIAA/ASME/SAE/ASEE Joint Propulsion Conference and Exhibit, Hartford, CT, 21–23 July 2008; received 6 October 2008; revision received 19 May 2009; accepted for publication 21 June 2009.

*Graduate Student Researcher, Department of Aerospace Engineering, 270 Ferst Drive. Student Member AIAA.

†Assistant Professor, Department of Aerospace Engineering, 270 Ferst Drive, Atlanta, GA 30332. Member AIAA.

‡Data available online at http://www.varianinc.com/cgi-bin/nav?products/vacuum/measure/index&cid=IPMHIKJQFO [retrieved 19 May 2009].

Table 1 Facility pressure as a function of mass flow rate

Mass flow rate, mg/s	Ar operating pressure, torr	Xe operating pressure, torr
0.5	2.0×10^{-5}	4.3×10^{-5}
1.5	2.4×10^{-5}	4.8×10^{-5}
2.5	2.7×10^{-5}	5.2×10^{-5}
3.0	3.0×10^{-5}	5.6×10^{-5}

G100TF ionization gauge with a KJLC model IG2200 ionization gauge controller and a KJLC Accu-Quad residual gas analyzer (RGA), both located on the top of the chamber. The RGA has a detection limit of 5×10^{-14} torr and an accuracy of $\pm 10\%$, as reported by KJLC.

Table 1 shows the VTF operating pressure for each flow rate, as measured by the facility pressure gauge. Previous investigations show that these facility back pressures are lower than typical pressures for helicon experiments [19,26,27]. The chamber pressures listed are the indicated pressures from the RGA. The pressures indicated in Table 1 are for three of the six diffusion pumps in operation.

B. Annular Helicon Plasma Source

Figure 1 shows the AH plasma source and subsystems used in this experiment. The annular ionization chamber is composed of two concentric Pyrex tubes with inner diameters of 120 and 171 mm and thicknesses of 3 and 3.5 mm, respectively. A left-twist helical pitch antenna is wrapped on the outside of the outer tube, with a separate left-twist helical pitch antenna wrapped on the inside of the inner tube. The antennas are constructed from $\frac{1}{2}$-in.-wide by $\frac{1}{8}$-in.-thick copper strips and are wrapped in 3M glass cloth electrical tape to prevent direct contact of the plasma with the antennas. The copper strips are brazed together to form the antenna, which provides a clean electrical connection between antenna segments. The outer antenna has an outer diameter of 186 mm and a length of 192.7 mm. The inner antenna has an outer diameter of 110 mm and a length of 192.7 mm. The antenna inlet plane is located parallel to the inlet plane of the first solenoid, which places the antenna in a region of constant axial magnetic field, as recommended by Yano et al. [23] and Yano and Walker [25]. The overall device length is much longer than the theorized requirement to allow investigation of the effects of solenoid location, solenoid spacing, and antenna location relative to solenoids on device performance. Although analysis of downstream plasma properties may allow new insights into device performance and potential benefits, it is likely that a practical AH could be significantly shorter in overall length, on the order of twice the antenna length or less.

The AH propellant distributor is a sealed stainless steel diffuser with two diametrically opposite inlets on the rear. The inner diameter of the propellant distributor is 130 mm, the outer diameter is 160 mm, and the depth is 25.4 mm. Propellant leaves the distributor through 36 holes of 0.39 mm diameter spaced 10 deg apart. High-purity (99.9995% pure) argon or xenon gas is fed through an MKS 1179JA mass flow controller through stainless steel feed lines to the propellant distributor. A custom fixed-volume mass flow calibration system is employed to calibrate the mass flow controller. The mass flow controller has an accuracy of $\pm 1\%$ of full scale, which varies based on the maximum desired flow rate for the test. For this experiment, full-scale flow is 7.43 mg/s for argon and 24.4 mg/s for xenon.

The AH requires power for the inner and outer antennas as well as to the magnet solenoids. RF power is provided to each antenna in phase via the RF power system shown in Fig. 1. The antennas are each cut at the center of one of the legs, as described by Chen [19,20] and Chi et al. [28]. The RF power input leads connect at the downstream end of each helical antenna and the return leads connect at the upstream end. The antennas are set such that the legs twist on top of one another, which allows for optimal coupling of the antennas to the plasma [23]. The antenna leads carry current in the same direction. AH theory and past experimental studies show that in-phase antennas with current flow in the same direction produce the best coupling to the plasma [21–23,25].

The Acom 2000A linear amplifier produces RF power up to 2500 W steady state. The RF forward and reflected power levels are measured with a Bird 43 Thruline wattmeter and the Palstar AT5K matching network internal power gauge. The Bird 43 Thruline wattmeter has an accuracy of $\pm 5\%$ of full scale, and the Palstar AT5K wattmeter has an accuracy of $\pm 10\%$ of full scale. For this analysis, full scale is set to 2500 W by the Bird wattmeter inductor insert. The RF power system is enclosed in a Faraday cage to prevent RF radiation from the system components. The cabinet is cooled through electromagnetic interference (EMI)-shielded ports and is grounded to the vacuum chamber.

The Palstar AT5K 3500 W L-type matching network, which has a native impedance of 50 Ω, matches the impedance of the amplifier to the antennas. The impedance of the antennas is extremely low and purely resistive, which means that no inductive reactance is present. For this antenna configuration, the resistance is approximately 3 Ω without plasma present. To minimize radiation outside of the antenna and ionization channel (i.e., reduce reflected and lost power), the impedance of all cables and feedthroughs is 50 Ω. The RF reflected power is less than 1% of the forward power for all measurements taken, which indicates that the matching network is well tuned to the antennas.

Five solenoids (powered by an Electronic Measurements, Inc., 60 kW power supply) generate a steady-state axial magnetic field of up to 450 G. The solenoid current is measured with a Fluke 337 clamp-on ammeter with an accuracy of $\pm 2\%$. The power leads to the antennas and solenoids are EMI-shielded with tinned copper mesh to eliminate RF radiation into and out of the wire. To reduce RF signal propagation up the power leads, $\frac{1}{2}$- and $\frac{1}{4}$-in.-diam ferrites are used.

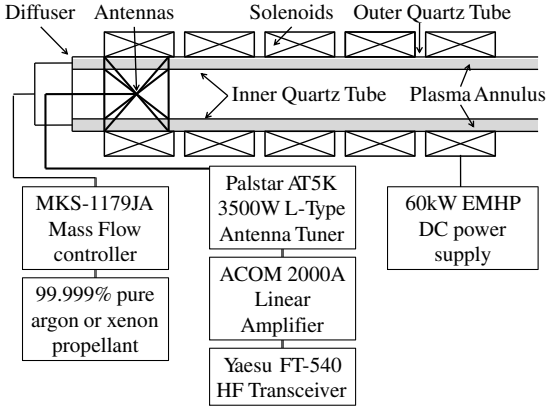

Fig. 1 Schematic of annular helicon subsystems. The annular helicon ionization chamber (shaded) has a 171 mm outer diameter, 120 mm inner diameter, and a 1626 mm length.

C. Hiden Analytical Langmuir Probe

All ion number density, electron temperature, and electron energy distribution function (EEDF) measurements are taken with the Hiden Analytical ESPion Langmuir probe system. Chen [29] shows that this system is suitable for high-density magnetized RF plasma measurements. The probe is mounted to a 1.5 by 1.5 m Parker Daedel automated motion control system to provide linear axial and radial motions with an accuracy of ± 1 μm. The probe uses a compensation electrode tuned to remove RF signals throughout the 2–15 MHz RF range used in these tests. A 0.15-mm-diam, 10-mm-long tungsten probe tip is used as a current collector. A reference electrode is positioned behind the filament to provide a return path for current collected from the plasma. This corrects measurements for changes in the plasma potential relative to the system ground potential [20,29–31]. The probe filament is mounted to the end of an 810-mm-long ceramic sting, which contains the RF-compensation inductors. The inductors are cooled through the umbilical by a forced-air circulation system.

The Hiden software, connected to the control head, collects I-V curves from the plasma. The Hiden probe measures the electron and ion currents to provide electron and ion number density measurements [30]. The Hiden ESPion system contains a data analysis tool that uses orbital-motion-limited and Allen et al. analysis techniques as discussed in [30]. The probe has an error of $\pm 50\%$ for electron and ion number densities and $\pm 20\%$ for electron temperature [29,32]. All diagnostic equipment is grounded to its own separate ground within the facility to prevent RF interference in measurements.

The calculation of the EEDF by the Druyvesteyn method is performed automatically in the Hiden software and is accurate to $\pm 50\%$ [30]. The second derivative method requires a smooth I-V trace to produce accurate results [32]. Any increases in the second derivative of the I-V trace can produce false peaks in the EEDF. To allow numerical integration, each I-V trace is taken in 0.1 V increments from -15 to 90 V. At each operating point, the average of 10 I-V traces is smoothed with a 25-point smoothing filter and used as the input to the Druyvesteyn method [30,33].

III. Experimental Data

The ion number density and electron temperature of the AH plasma are characterized over a broad range of operating conditions with the RF-compensated Langmuir probe. Axial profiles of ion number density and electron temperature are important to determine the optimal location at which to mate the AH to the HET. Radial profiles of ion number density and electron temperature are important to measure to ensure that a HET located in the exhaust of the helicon will receive uniform high-density plasma for acceleration. Helicons display rapid increases in ion number density as RF forward power increases when mode shifts occur. Therefore, ion number density profiles are taken as a function of RF forward power at several operating conditions to determine a threshold for each observed mode shift. Ion number density profiles are also taken as a function of RF to determine if the AH is tunable to a given propellant. If an optimal RF exists for a given propellant, this may allow the AH to be used to efficiently ionize a multitude of propellants. The coordinate system for these measurements locates the downstream end of the antenna at an axial location of 0 mm, and the exhaust plane of the device is at an axial location of 480 mm. The data points have been connected in Figs. 2–12 for clarity.

A. Axial Profile

Figures 2 and 3 show the ion number density and electron temperature versus axial location for argon propellant. These measurements are taken along the centerline of the annular channel, at the right center of the exhaust plane. Figure 2 shows that for the 0 and 200 G magnetic field cases, the ion number density increases as the distance from the antenna increases: it rises from approximately 5.0×10^{16} to over 1.1×10^{17} m^{-3}. For a magnetic field strength of 400 G, the ion number density starts at 2.6×10^{17} m^{-3} and decreases as the distance from the antenna increases. Figure 3 shows that the 200 G magnetic field has the highest average electron temperatures, approximately 5.7 eV, and the 400 G magnetic field case has the lowest electron temperatures, with an average of approximately 2.5 eV.

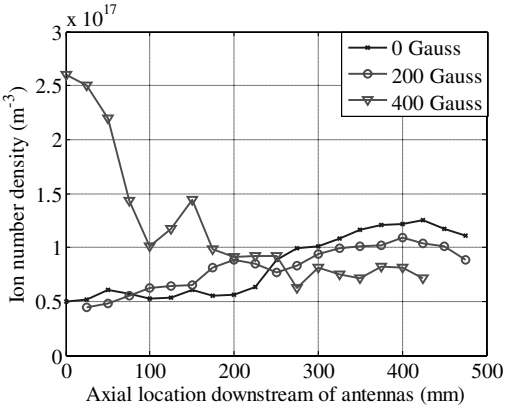

Fig. 2 Ion number density versus axial location; 7 MHz RF frequency, 1 kW RF forward power, 3 mg/s Ar mass flow rate, and 3.0×10^{-5} torr of Ar operating pressure.

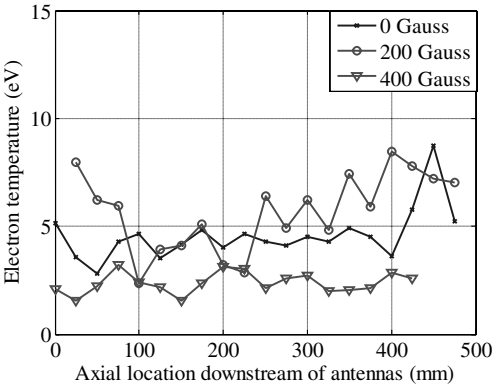

Fig. 3 Electron temperature versus axial location; 7 MHz RF frequency, 1 kW RF forward power, 3 mg/s Ar mass flow rate, and 3.0×10^{-5} torr of Ar operating pressure.

B. Radial Profile

Figures 4 and 5 show the ion number density and electron temperature versus radial location for argon propellant. These measurements are taken at an axial location of 0 mm, at the right center of the exhaust channel as viewed from downstream. The inner wall of the annulus is located at a radial location of 0 mm, and the

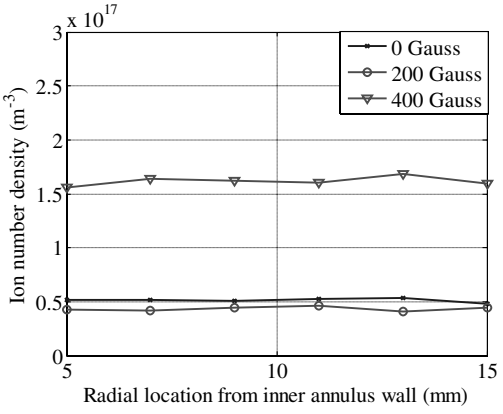

Fig. 4 Ion number density versus radial location; 0 mm downstream of antennas, 7 MHz RF frequency, 1 kW RF forward power, 3 mg/s Ar mass flow rate, and 3.0×10^{-5} torr of Ar operating pressure.

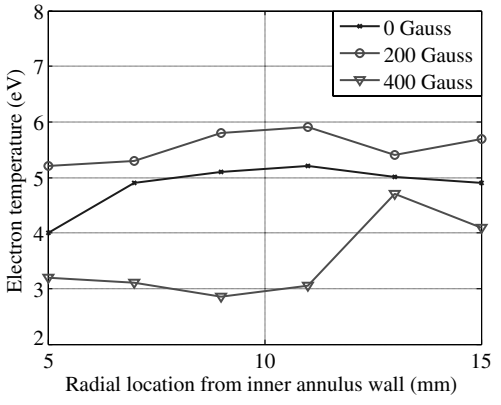

Fig. 5 Electron temperature versus radial location; 0 mm downstream of antennas, 7 MHz RF frequency, 1 kW RF forward power, 3 mg/s Ar mass flow rate.

outer wall of the annulus is at a radial location of 21.5 mm. Figure 4 shows that the maximum ion number density is generated at a 400 G magnetic field. For all magnetic field strengths, the ion number density is effectively constant across the channel. Figure 5 shows that the lowest electron temperature of 2.8 eV is measured at the 400 G case, and the highest is 5.9 eV at 200 G.

C. RF Power

Figures 6 and 7 show the ion number density and electron temperature as a function of RF power. These measurements are taken at an axial location of 250 mm, on the channel centerline, with argon propellant. This location is just past the second magnetic solenoid and is the location for the highest ion number density from previous investigations [21–23]. Figure 6 shows that the 0 G magnetic field case exhibits the highest ion number density at power levels less than 800 W, after which the 200 G case trends highest, with a peak of 2.3×10^{17} m^{-3}. The other ion number density profiles follow similar trends and are between 5.1×10^{16} and 2.3×10^{17} m^{-3}. Figure 7 shows that the 400 G case has the lowest electron temperature at 1.7 eV as well as the highest at 7.1 eV.

D. Frequency Variation

Figures 8 and 9 show the ion number density and electron temperature as a function of RF. These measurements are taken at an axial location of 0 mm, on the channel centerline, with argon propellant. Figure 2 shows that this location is the peak ion number density for the highest magnetic field case. Figure 8 shows effectively constant ion number densities, all within 18% of the average of 1.2×10^{17} m^{-3} for the 500 W RF power case. The 1000 W RF power case shows similar trends; however, between 6 and 9 MHz and again at 12 MHz, the ion number density is significantly higher, with a peak at 1.9×10^{17} m^{-3} at 8 MHz, a 62% increase from the mean level, which is larger than the error limits of the measurement system. Figure 9 shows that the electron temperature for the 500 W RF power case ranges from a maximum of 14 eV to a minimum of 8 eV, and the 1000 W RF power case ranges from a maximum of 8 eV to a minimum of 1 eV. The electron temperature for the 8 MHz case does not follow established trends, for a large increase in ion number density would typically be accompanied by a decrease in electron temperature; however, this is not always observed in measurements of this type [9,32,34].

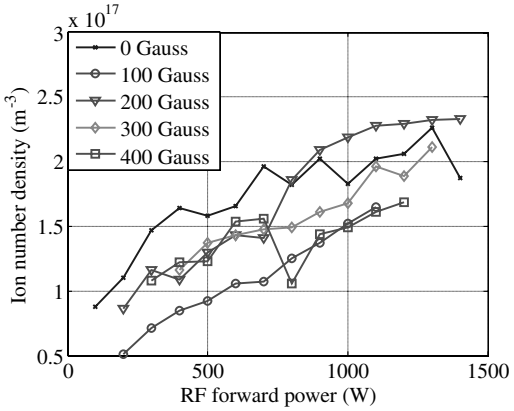

Fig. 6 Ion number density versus RF forward power; 250 mm downstream of antennas, 7 MHz RF frequency, 1 kW RF forward power, 3 mg/s Ar mass flow rate, and 3.0×10^{-5} torr of Ar operating pressure.

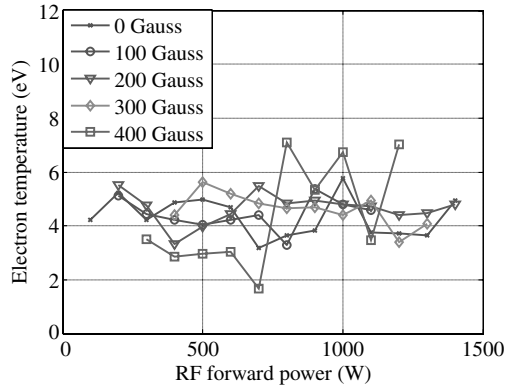

Fig. 7 Electron temperature versus RF forward power; 250 mm downstream of antennas, 7 MHz RF frequency, 1 kW RF forward power, 3 mg/s Ar mass flow rate, and 3.0×10^{-5} torr of Ar operating pressure.

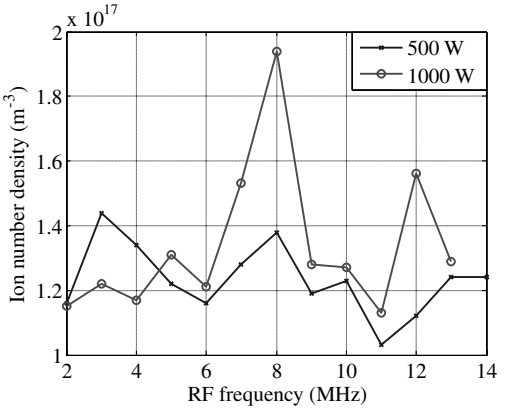

Fig. 8 Ion number density versus RF; 0 mm downstream of antennas, 1 kW RF forward power, 400 G B-field, 3 mg/s Ar mass flow rate, and 3.0×10^{-5} torr of Ar operating pressure.

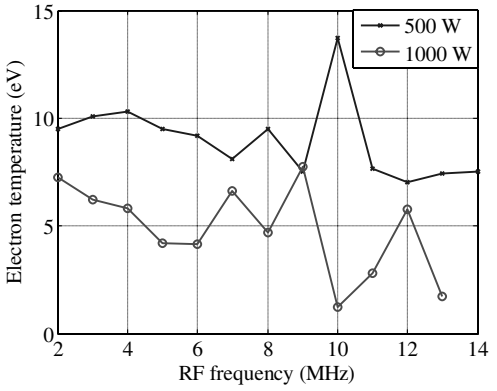

Fig. 9 Electron temperature versus RF; 0 mm downstream of antennas, 1 kW RF forward power, 400 G B-field, 3 mg/s Ar mass flow rate, and 3.0×10^{-5} torr of Ar operating pressure.

E. Electron Energy Distribution Functions

Figure 10 shows the EEDF at several selected RFs. These measurements are taken at an axial location of 0 mm, on the channel centerline, at 1 kW of RF power, and at a magnetic field strength of 400 G. This axial location is selected as it is the peak ion number density from Fig. 2. The magnitude and location of the peak in the EEDF are a strong function of the RF. The value of the primary peak of the EEDF varies from 3.7 eV for 13 MHz to 15 eV for 11 MHz.

F. Axial Profile: Xenon

Figures 11 and 12 show axial profiles of the ion number density and electron temperature for xenon propellant. These measurements are taken at a radial location on the channel centerline, at a magnetic field strength of 200 G, and are included with that of argon from Fig. 2 for comparison. Figure 11 shows that xenon peaks at an ion number density of 2.4×10^{17} m^{-3} at an axial location of 0 mm and has a minimum value of 4.0×10^{16} m^{-3} at an axial location of 75 mm.

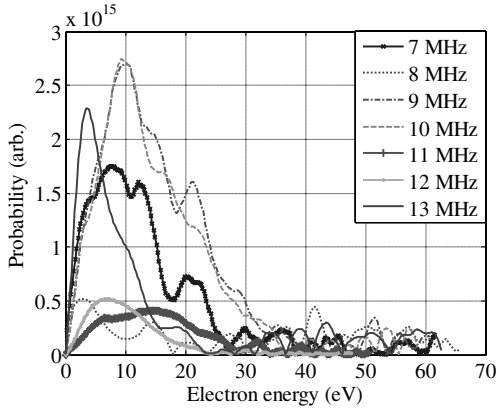

Fig. 10 EEDF at selected RFs; 0 mm downstream of antennas, 1 kW RF forward power, 400 G B-field, 3 mg/s Ar mass flow rate, and 3.0×10^{-5} torr of Ar operating pressure.

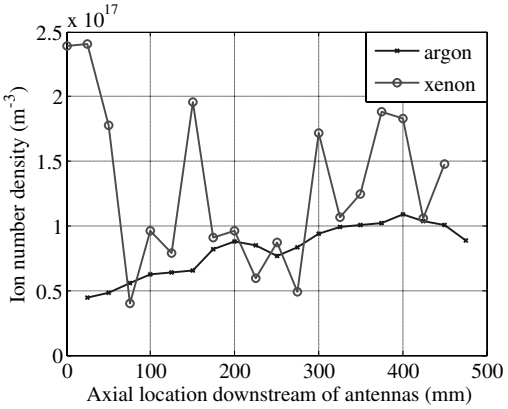

Fig. 11 Ion number density versus axial location; 7 MHz RF frequency, 1 kW RF forward power, 200 G B-field, 3 mg/s Ar and Xe mass flow rate, along channel centerline, 3.0×10^{-5} torr of Ar operating pressure, and 5.6×10^{-5} torr of Xe operating pressure.

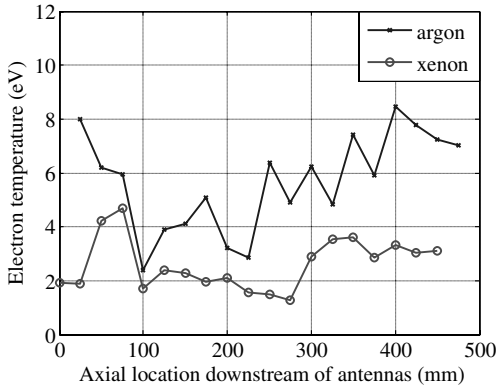

Fig. 12 Electron temperature versus axial location; 7 MHz RF frequency, 1 kW RF forward power, 200 G B-field, 3 mg/s Ar and Xe mass flow rate, along channel centerline, 3.0×10^{-5} torr of Ar operating pressure, and 5.6×10^{-5} torr of Xe operating pressure.

IV. Discussion

The RF-compensated Langmuir probe data establish a baseline for AH plasma generation across the range of operating conditions measured. The trends in the data are now examined to determine their correlation with previous results and with coupling modes observed and to determine the appropriateness of this plasma source as an ionization stage for the HET.

To understand the mechanisms behind the trends indicated in the measurements, plasma parameters are calculated for each trend. The gyro radii calculations for measurements with argon indicate that the electrons are magnetized for the 200 and 400 G magnetic field cases, but the ions are not.

The axial ion number density trends shown in Figs. 2 and 3 indicate that there could be a different coupling mechanism that causes improved RF power deposition into the plasma at 400 G magnetic field strength. The dependence of the ion number density on magnetic field could indicate that a helicon wave mode is excited due to the magnetic field coupling to the RF. However, the ion number densities are lower than most helicon modes are known to excite, and so the perpendicular and parallel wave numbers must be ascertained by B-dot probe measurements to confirm if a helicon mode is excited [28]. The power density for this device is at maximum 4.3×10^4 W/m^3, which is comparable with similar cylindrical helicon devices [27,35]. This indicates that the decrease in ion number density is not attributable to a lack of power density. The electron temperature profiles show that the higher-ion-number-density cases trend toward the lowest electron temperatures, which is the most efficient method of ionization, as the greatest percentage of input energy goes to ionization rather than electron energy. The 0 and 200 G magnetic field cases trend toward the highest electron temperatures, especially near the exit plane of the device. This may be an indication of capacitive coupling for the 0 and 200 G magnetic field cases.

The radial ion number density and electron temperature profiles shown in Figs. 4 and 5 indicate that the ion density is constant across the radius of the device, well within the error limits of the Langmuir probe. An ion number density peak on the annular channel centerline with low density near the walls is desired for efficient HET operation. The axial magnetic field strength is nearly constant across the channel, which rules out inner wall losses as the cause of the decreased ion number densities on the inner wall. Yano et al. [23] and Yano and Walker [25] predict a more favorable radial ion number density profile for HET operation when the annular plasma is in the annular helicon wave mode (i.e., low ion number density near the walls).

Ion number density and electron temperature as a function of RF forward power is shown in Figs. 6 and 7. These indicate that the highest ion number densities can be reached in the 200 G configuration, up to 2.3×10^{17} m^{-3} at this location. Each data set shows an increase in ion number density with RF forward power and shows that the ion number density does not show a trend with magnetic field strength in this coupling mode. The electron temperatures range between 3.5 and 5.5 eV, with the exception of the 400 G magnetic field case, which spikes to above 6 eV at RF power levels above 700 W. These data points may be exaggerated by the current conduction to the plasma from the probe. At high bias voltages, the probe can emit its own electrons as well as generate a ground loop within the plasma [30]. Without accompanied increases in ion number density, the jumps in electron temperature do not indicate a shift to helicon mode [19,20,28,29,31,36].

The RF dependence of ion number density and electron temperature shown in Figs. 8 and 9 are required to understand the benefits of a helicon plasma source over other ionization options. For a given propellant, there may exist an optimal frequency at which the AH will produce a maximum ion number density. The RF trend shows that for argon propellant, the highest ion number density of 1.9×10^{17} m^{-3} is produced at 8 MHz for the 1000 W case, whereas for the 500 W case, the ion number density is lower (an average of 1.3×10^{17} m^{-3}) and is roughly independent of RF because it is within the error limits of the Langmuir probe. At 7 and 12 MHz RF, the peak ion number density is 1.5×10^{17} m^{-3}, which is within the error limits of the 8 MHz data point. This shows that the optimal frequency exists between 6 and 9 MHz or at 12 MHz for this configuration, even though the increase in ion number density is not accompanied by a decrease in electron temperature [9,32,34]. These results indicate that the optimal frequency to maximize plasma generation varies with input power, and this frequency should be determined for a helicon device to reach the optimal operating

condition for efficient plasma generation. Further investigation must be performed to determine the effects of device configuration, magnetic field, and other variables on this frequency and whether they are propellant-specific.

The EEDFs measured depict a single-hump structure for most operating conditions. The EEDF trends measured in Fig. 10 show that the EEDF peak and shape vary with RF. The relative amplitude of the primary peak in the EEDF tends to be higher for the 7, 9, 10, and 13 MHz frequencies, whereas the 8, 11, and 12 MHz cases indicate much lower relative probabilities. This points to the 8, 11, and 12 MHz cases as being able to bring electrons to higher energies than the other frequencies shown; however, the peak values and relative intensities do not correlate with the trends in ion number density or electron temperature, which is similar to past studies [6,9,12,13,32,34]. The EEDFs measured have larger energy dependence than those in previous works [9,32,37]. The 8 and 12 MHz EEDFs shown in Fig. 10 have much lower relative probabilities of the low energy peak than the other frequencies. This correlates to the 8 and 12 MHz values shown in Fig. 8, which are the two ion number density peaks. This signifies that a correlation may exist between ion number density and relative probability of the EEDF, as all the frequencies measured follow the trend except 11 MHz.

Figures 11 and 12 show increased ion number densities and electron temperatures for xenon over argon, with a peak value of 2.4×10^{17} m^{-3} and 1.1×10^{17} m^{-3} for xenon and argon, respectively. Xenon exhibits electron temperatures that are, on average, 55% lower and ion number densities that are, on average, 41% higher than those of argon at the same operating conditions. The xenon electron temperatures are significantly lower than those of argon, which indicates that the xenon plasma is more efficiently ionized. The lower electron temperature and higher ion number density for xenon can be attributed to more complete ionization due to the lower first ionization potential of xenon: 12.1 eV as opposed to 15.7 eV for argon.

For the AH plasma source to be an effective ionization stage for the HET, it must achieve an average ionization cost per accelerated ion that is less than that achieved by state-of-the-art HETs. For example, if one assumes that most of the thermal power deposited into a HET results from inefficiencies in the ionization process, it can be inferred from previously published measurements that the ionization cost in the current SOA HET is approximately 120 eV for operation on xenon, which has a first ionization potential of 12.1 eV [38].

In this study, it is not possible to determine the ionization cost of each accelerated ion, because the plasma generated in the AH is nearly stationary. Nonetheless, we can attempt to infer the ionization cost based on our measurements and previous work on helicon plasma sources. Squire et al. [39] show that a conservative estimate of the ionization cost of each electron–ion pair generated by a helicon plasma source with argon is 80 eV. Thus, the helicon plasma source achieves an ion–electron pair ionization cost that is only 5.1 times greater than the first ionization potential of argon: 15.7596 eV [36]. This is in fair agreement with early claims that the helicon plasma source realizes ionization costs close to the first ionization potential of the working gas [40].

If we assume that the AH plasma source can achieve similar performance on xenon, then the average ionization cost of each accelerated xenon ion is 61.7 eV. The theoretical efficiency of a standard HET thruster with a 120 eV ionization cost (with η_u of 90%, γ of 95%, V_{NC} of 15 V, and a V_B of 100 V) is 35%. If the ionization cost is reduced to 61.7 eV, the efficiency jumps to 46%. Thus, the ability of an AH to achieve ionization costs on xenon similar to those with the cylindrical helicon on argon could lead to an 11% increase in HET efficiency in the high-thrust-to-power operating regime.

The conditions in the annular plasma source support the possibility of a reduction in the xenon ionization cost. The measurements of electron number density and electron temperature presented in this work for the AH plasma source are similar to those taken in cylindrical helicons at comparable operating conditions [41]. Xenon has an ionization cost that is 24% less than that of argon. The xenon atom (molecular weight of 131.30) is significantly larger than argon (molecular weight of 39.948). Thus, it should have an electron-neutral ionization cross section that is larger than argon, which will lead to a greater number of ionization events than argon has for the same electron population. Furthermore, the more massive xenon atom will have a greater residence time in the ionization zone than argon has for an equivalent mass flow rate, which should also increase the probability of an electron-neutral ionization collision. These facts lead one to believe that AH plasma source will achieve an ionization cost per accelerated ion that is only a few times greater than the first ionization potential of xenon.

Based on the characterization, the optimal location to mate a Hall thruster is at the antenna exit plane, which also minimizes device size and therefore mass. At this location, the plasma also has the highest ion number density and lowest electron temperature for xenon and argon propellants. The target ion number density for a two-stage HET is in the range of 1.2×10^{17} to 1.6×10^{18} m^{-3} for xenon propellant. The AH produces the ion number density levels required for sustained two-stage HET thruster operation.

V. Conclusions

The peak ion number density recorded for the AH is 2.6×10^{17} m^{-3} for argon and 2.4×10^{17} m^{-3} for xenon, which occurs at the exhaust plane of the antennas, at an RF of 7 MHz, RF forward power of 1000 W, and at a magnetic field of 400 G. Axial profiles of ion number density show that the density behavior of the device is not easily determined; however, the magnetic field effects on ion number density suggest that a helicon wave mode may be present. RF profiles show that the optimal frequency for maximum ion number density for argon propellant is between 6 and 9 MHz or at 12 MHz. The EEDF is calculated for several RFs, and it is shown that the peak and width of the EEDF varies by selection of the RF for a given propellant. Xenon propellant yields the highest ion number densities at the lowest electron temperatures. The AH produces high-density plasma with a constant radial profile at an axial location of 0 mm. At this location, the maximum density plasma will be ejected into the acceleration stage of the proposed two-stage HET. The target ion number density for laboratory HET operation on xenon propellant, in the range of 1.2×10^{17} to 1.6×10^{18} m^{-3}, is met by the device.

Acknowledgments

This research is supported by the U.S. Air Force Office of Scientific Research grant FA9550-07-1-0137. Mitat Birkan is the contract monitor. The authors wish to thank the NASA Marshall Space Flight Center for supplying the radio frequency power system, and Scott Elliott and Scott Moseley of the Georgia Institute of Technology Aerospace Engineering Machine Shop for fabrication of hardware.

References

[1] Hofer, R. R., and Jankovsky, R. S., "A Hall Thruster Performance Model Incorporating the Effect of a Multi-Charged Plasma," 37th Joint Propulsion Conference and Exhibit, AIAA Paper 2001-3322, Salt Lake City, UT, July 2001.

[2] Hofer, R. R., Jankovsky, R. S., and Gallimore, A. D., "High-Specific Impulse Hall Thrusters, Part 1: Influence of Current Density and Magnetic Field," *Journal of Propulsion and Power*, Vol. 22, No. 4, Aug. 2006, pp. 721–731. doi:10.2514/1.15952

[3] Beal, B. E., Gallimore, A. D., Morris, D. P., Davis, C., and Lemmer, K. M., "Development of an Annular Helicon Source for Electric Propulsion Applications," 42nd Joint Propulsion Conference and Exhibit, AIAA Paper 2006-4841, Sacramento, CA, July 2006.

[4] Jacobson, D. T., Jankovsky, R. S., Rawlin, V. K., and Manzella, D. H., "High Voltage TAL Performance," 37th Joint Propulsion Conference and Exhibit, AIAA 2001-3777, Salt Lake City, UT, July 2001.

[5] Beal, B. E., and Gallimore, A. D., "Development of the Linear Gridless Ion Thruster," 37th Joint Propulsion Conference and Exhibit, AIAA Paper 2001-3649, Salt Lake City, UT, July 2001.

[6] Fruchtman, A., Fitsch, N. J., and Raitses, Y., "Hall Thruster with Absorbing Electrodes," 36th Joint Propulsion Conference and Exhibit, AIAA Paper 2000-3659, Huntsville, AL, July 2000.

[7] Solodukhin, A. E., Semenkin, A. V., Tverdohlebov, S. O., and Kochgerin, A. V., "Parameters of D-80 Anode Layer Thruster in One- and Two-Stage Operation Modes," 27th International Electric Propulsion Conference, Electric Rocket Propulsion Society, Paper 2001-032, Pasadena, CA, Oct. 2001.

[8] Pote, B., and Tedrake, R., "Performance of a High Specific Impulse Hall Thruster," 27th International Electric Propulsion Conference, Electric Rocket Propulsion Society, Paper 2001-35, Pasadena, CA, Oct. 2001.

[9] Hofer, R. R., "Development and Characterization of High-Efficiency, High-Specific Impulse Xenon Hall Thrusters," Ph.D. Thesis, Univ. of Michigan, Dept. of Aerospace Engineering, Ann Arbor, MI, 2004.

[10] Szabo, J., Warner, N., and Martinez-Sanchez, M., "Instrumentation and Modeling of a High Specific Impulse Hall Thruster," 38th Joint Propulsion Conference and Exhibit, AIAA Paper 2002-4248, Indianapolis IN, July 2002.

[11] Fisch, N. J., Raitses, Y., Litvak, A. A., and Dorf, L. A., "Design and Operation of Hall Thruster with Segmented Electrodes," 35th Joint Propulsion Conference and Exhibit, AIAA Paper 99-2572, Los Angeles, July 1999.

[12] Fisch, N. J., Raitses, Y., Litvak, A. A., and Dorf, L. A., "Segmented Electrode Hall Thruster Operation in Single and Two Stage Regimes," 26th International Electric Propulsion Conference, Electric Rocket Propulsion Society, Paper 99-101, Kitakyushu, Japan, Oct. 1999.

[13] Fisch, N. J., Raitses, Y., and Litvak, A. A., "Variable Operation of Hall Thruster with Multiple Segmented Electrodes," *Journal of Applied Physics*, Vol. 89, No. 4, Feb. 2001, pp. 2040–2046. doi:10.1063/1.1337919

[14] Molina-Morales, P., Kuninaka, H., Toki, K., and Arakawa, Y., "Preliminary Study of an ECR Discharge Hall Thruster," 27th International Electric Propulsion Conference, Electric Rocket Propulsion Society, Paper 2001-069, Pasadena, CA, Oct. 2001.

[15] Hofer, R. R., Peterson, P. Y., and Gallimore, A. D., "A High Specific Impulse Two-Stage Hall Thruster with Plasma Lens Focusing," 27th International Electric Propulsion Conference, Electric Rocket Propulsion Society, Paper 2001-036, Pasadena, CA, Oct. 2001.

[16] Linnell, J. A., and Gallimore, A. D., "Internal Plasma Structure Measurements of a Hall Thruster Using Xenon and Krypton," 29th International Electric Propulsion Conference, Electric Rocket Propulsion Society, Paper 2005-024, Princeton, NJ, 2005.

[17] Linnell, J. A., and Gallimore, A. D., "Internal Plasma Structure Measurements of a Hall Thruster Using Plasma Lens Focusing," 41st Joint Propulsion Conference, AIAA Paper 2005-4402, Tucson, AZ, July 2005.

[18] Linnell, J. A., and Gallimore, A. D., "Internal Langmuir Probe Mapping of a Hall Thruster with Xenon and Krypton Propellant," 42nd Joint Propulsion Conference and Exhibit, AIAA Paper 2006-4470, Sacramento, CA, July 2006.

[19] Chen, F. F., "Plasma Ionization by Helicon Waves," *Plasma Physics and Controlled Fusion*, Vol. 33, No. 4, 1991, pp. 339–364. doi:10.1088/0741-3335/33/4/006

[20] Chen, F. F., "Helicon Wave Plasma Sources," *Proceedings of the International Conference on Plasma Physics*, Vol. 2, World Scientific, Singapore, 1987, p. 1378.

[21] Palmer, D., Akinli, C., and Walker, M. L. R., "Characterization of an Annular Helicon Plasma Source," 30th International Electric Propulsion Conference, Electric Rocket Propulsion Society, Paper 2007-202, Florence, Italy, Sept. 2007.

[22] Palmer, D., and Walker, M. L. R., "Operation of an Annular Helicon Plasma Source," 44th Joint Propulsion Conference and Exhibit, AIAA Paper 2008-4926, Hartford, CT, July 2008.

[23] Yano, M., Palmer, D., Williams, L., and Walker, M. L. R., "Design and Operation of an Annular Helicon Plasma Source," 43rd Joint Propulsion Conference, AIAA Paper 2007-5309, Cincinnati, OH, July 2007.

[24] Zhurin, V. V., Kaufman, H. R., and Robinson, R. S., "Physics of Closed Drift Thrusters," *Plasma Sources Science and Technology* , Vol. 8, No. 1, Feb. 1999, pp. R1–R20. doi:10.1088/0963-0252/8/1/021

[25] Yano, M., and Walker, M. L. R., "Plasma Ionization by Annularly-Bounded Helicon Waves," *Physics of Plasmas*, Vol. 13, No. 6, June 2006, Paper 063501 1-5. doi:10.1063/1.2207125

[26] Randolph, T., Kim, V., Kaufman, H., Kozubsky, K., Zhurin, V. V., and Day, M., "Facility Effects on Stationary Plasma Thruster Testing," 23rd International Electric Propulsion Conference, Electric Rocket Propulsion Society, Paper 93-093, Seattle, WA, Sept. 1993.

[27] West, M., Charles, C., and Boswell, R. W., "Testing a Helicon Double Layer Thruster Immersed in a Space-Simulation Chamber," *Journal of Propulsion and Power*, Vol. 24, No. 1, Jan.–Feb. 2008, pp. 134–141. doi:10.2514/1.31414

[28] Chi, K.-K., Sheridan, T. E., and Boswell, R. W., "Resonant Cavity Modes of a Bounded Helicon Discharge," *Plasma Sources Science and Technology* , Vol. 8, No. 3, 1999, pp. 421–431. doi:10.1088/0963-0252/8/3/312

[29] Chen, F. F., "Langmuir Probe Analysis for High-Density Plasmas," *Physics of Plasmas*, Vol. 8, No. 6, June 2001, pp. 3029–3041. doi:10.1063/1.1368874

[30] *Handbook of Plasma Diagnostics*, Hiden Analytical, Ltd., Warrington, England, U.K., 2000.

[31] Chen, F. F., "Time-Varying Impedance of the Sheath on a Probe in an RF Plasma," *Plasma Sources Science and Technology* , Vol. 15, No. 4, 2006, pp. 773–782. doi:10.1088/0963-0252/15/4/022

[32] Herman, D., "The Use of Electrostatic Probes to Characterize the Discharge Plasma Structure and Identify Discharge Cathode Erosion Mechanisms in Ring-Cusp Ion Thrusters," Ph.D. Thesis, Univ. of Michigan, Dept. of Aerospace Engineering, Ann Arbor, MI, 2005.

[33] Druyvestyn, M. J., "Der Neidervoltbogen," *Zeitschrift für Physik*, Vol. 64, 1930, pp. 781–798. doi:10.1007/BF01773007

[34] Peterson, P. Y., "The Development and Characterization of a Two-Stage Hybrid Hall/Ion Thruster," Ph.D. Thesis, Univ. of Michigan, Dept. of Aerospace Engineering, Ann Arbor, MI, 2004.

[35] Sudit, I. D., and Chen, F. F., "Rf Compensated Probes for High-Density Discharges," *Plasma Sources Science and Technology* , Vol. 3, No. 2, May 1994, pp. 162–168. doi:10.1088/0963-0252/3/2/006

[36] Chen, F. F., *Plasma Physics and Controlled Fusion*, 2nd ed., Vol. 1, Springer Science, New York, 1983.

[37] Bibinov, N., Halfmann, H., and Awakowicz, P., "Determination of the Electron Energy Distribution Function Via Optical Emission Spectroscopy and a Langmuir Probe in an ICP," *Plasma Sources Science and Technology* , Vol. 17, No. 3, May 2008, p. 7. doi:10.1088/0963-0252/17/3/035004

[38] de Grys, K. H., and Rayburn, Haas, J. M., "Study of Power Loss Mechanisms in the BPT-4000 Hall Thruster," 39th Joint Propulsion Conference and Exhibit, AIAA Paper 2003-5277, Huntsville, AL, July 2003.

[39] Squire, J. P., Chang-Diaz, F. R., Glover, T. W., Carter, M. D., Cassady, L. D., Chancery, W. J., Jacobson, V. T., McCaskill, G. E., Sosen, C. S., Bering, E. A., Brukardt, M. S., and Longmier, B. W., "VASIMR Performance Measurements at Powers Exceeding 50 kW and Lunar Robotic Mission Applications," International Interdisciplinary Symposium on Gaseous and Liquid Plasmas, Akiu/Sendai, Japan, Sept. 2008.

[40] Chen, F. F., "Experiments on Helicon Plasma Sources," *Journal of Vacuum Science and Technology A (Vacuum, Surfaces, and Films)*, Vol. 10, No. 4, 1992, pp. 1389–1401. doi:10.1116/1.578256

[41] Charles, C., Boswell, R. W., and Lieberman, M. A., "Xenon Ion Beam Characterization in a Helicon Double Layer Thruster," *Applied Physics Letters*, Vol. 89, No. 26, Dec. 2006, p. 1503. doi:10.1063/1.2426881

R. Myers
Associate Editor